

Laboratory measurements of optical beams in young sea ice

J. S. Schoonmaker

Naval Ocean Systems Center, Code 742, San Diego, California 92152-5000

K. J. Voss

Physics Department, University of Miami, Coral Gables, Florida 33124

G. D. Gilbert

Naval Ocean Systems Center, Code 754, San Diego

Abstract

The optical properties of young sea ice (<20 cm thick) have been measured in the Naval Ocean Systems Center Ice Optics Lab. Measurements of the upwelling irradiance from the ice surface as a function of distance from the center of the beam spot (r in cm) were performed. The irradiance distributions were transformed to find the modulation transfer function (MTF) and beam spread function (BSF) as a function of ice thickness. The BSF could be approximated by $BSF(r, z) = \exp(-k_B z) \exp(-r^2/2 (r^2))$, with $k_B = 0.404 \text{ cm}^{-1}$ and $(r^2)^{1/2} = 0.105 z^{1.41}$ cm, where z is ice thickness (in cm). Angular radiance above the ice surface, resulting from a laser beam entering the ice from below, was measured as a function of ice thickness for a specific growth condition. The angular field followed a function of $L(\theta, z) = L(0, z) \cos^n(\theta)$, with $n = 8.1 z^{-0.71}$, while the peak value followed a Beer's law decay of the form $L(0, z) = L(0, 0) \exp(-0.514z)$.

Past measurements of the light fields and optics of Arctic sea ice have largely been concerned with irradiance fields in the Marginal Ice Zone, e.g. the natural light irradiance values, and the albedo and extinction properties of the ice (Perovich et al. 1986). The present work investigates laser beam rather than natural light propagation through young sea ice grown in a tank at the Ice Optics Laboratory (IOL) of the Naval Ocean Systems Center (NOSC). The tank ice is similar to new sea ice found in a newly opened lead in the Arctic ice pack where seawater is exposed to much colder air. We report on two laser beam propagation experiments through sea ice grown in a single ice growth sequence at an air temperature of -35°C as the IOL was brought into operation. The experiments were a beam spread function experiment (or BSF), which measured the spatial spreading of an approximately

Gaussian laser beam as it propagated through the ice into the air, and a beam scattering experiment, which measured the exiting radiance pattern produced as the laser beam was scattered and refracted into the air after passage through the ice.

To complete the study, our work in progress will measure ice grown at different air temperatures to simulate conditions affecting brine concentration in natural Arctic ice.

IOL facilities

Ice-growing facilities—The IOL is located in and uses the freezing system of the NOSC Arctic Submarine Laboratory. It consists of three interconnected insulated rooms. The temperature in two rooms can be controlled to $\pm 1^\circ$ from 25° to -40°C . One room is maintained at room temperature ($\sim 25^\circ\text{C}$) to house most of the instrumentation. The second room is kept cold and contains a cylindrical seawater tank in which sea ice is grown. A third intermediate room houses a similar tank for recirculation. The polyethylene plastic water tanks are 1.1 m in diameter and 1.2 m deep. The cold room tank has 30 cm of insulation on its sidewalls and rests on an insulating platform to reduce the heat flow from the sides and bottom of the tank. This allows ice to form from the water

Acknowledgments

Financial support for this work was provided by the Office of Naval Research under contract N00014-89-J-1043 and N00014-85-C-0730 and the Naval Ocean Systems Center Independent Research Program. We also acknowledge the help of Albert Chapin in data collection and Lawrence Oblinger and the staff of the Arctic Submarine Laboratory in running the laboratory for this experiment.

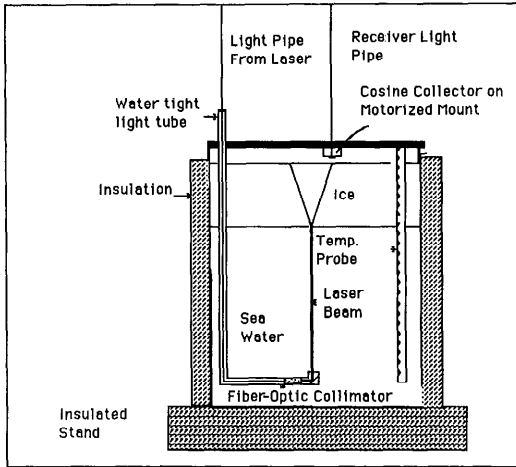


Fig. 1. Schematics of tank instrumentation, illustrated with measurement apparatus of the BSF experiment.

surface down as it would in the Arctic rather than on the tank sides. The cold room tank is plumbed to the recirculation tank. In this manner, control of water salinity is maintained while doubling the apparent volume of the water under the ice. Filtered seawater is supplied through a pipeline from the ocean off San Diego.

Light channeling—We used the same source and source lighting geometry for both experiments. The light source, a Spectra Physics 148 air-cooled argon ion laser in the laboratory room, provided blue light (488 nm) which was transmitted into the cold room and into the tank on multimode optical fiber. A fiber-optic beam collimator in the tank collimated the light into a 1-cm-diameter beam with ~ 9 -mrad divergence. The light exited the collimator in an upward direction and produced a spot of ~ 2 -cm diameter on the bottom of the ice; this size was chosen to be larger than the characteristic horizontal crystal size of sea ice. Although the light was polarized initially, after transmission through the fiber optic the polarization was $< 6\%$. The tank and instrumentation of the cold room are illustrated in Fig. 1.

Although the two experiments used the same light source, light collector geometries differed greatly and will be described in detail as each experimental arrangement is

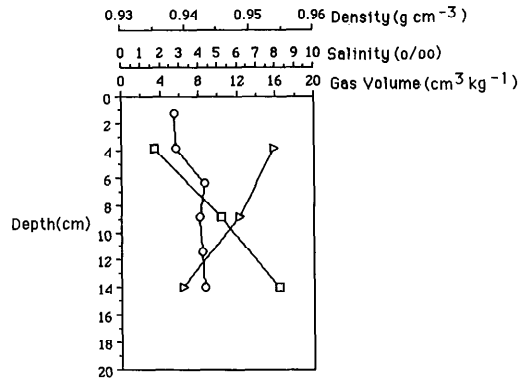


Fig. 2. Profile of the physical properties of the ice measured at completion of experiment. Density (Δ), entrapped gas (\square), and salinity (O) values are typical of natural sea ice.

presented. After collection, each experiment's photons were carried by dedicated optical fibers to a photomultiplier assembly (EG&G D-46AQ) in the warm instrument room for detection, digitization, and recording on computer disk.

The use of fiber optics alleviated two problem areas encountered in extreme cold. First, fiber optics allowed most instrumentation to operate at normal room temperature outside the cold room. Second, the use of fiber optics instead of conventional optical components such as mirrors, windows, lenses, etc. to transport the light eliminated exposed optical surfaces in the cold room. Cold optical surfaces readily condensed moisture in the air and immediately frosted. Before the use of optical fiber such frosting was a severe problem.

Auxiliary physical measurements—Ice thickness was monitored with a simple mechanical J-shaped gauge vertically frozen into the ice surface. The gauge was drawn upward against the ice-water interface with the length of the J stem protruding above the ice surface indicating thickness. Ice density and entrapped gas volume were found from ice sampled at three depths. Salinities were measured at six depths. Density, entrapped gas, and salinity values (Fig. 2) were typical of natural sea ice (Weeks and Ackley 1986). Measurement of the physical properties requires cutting up the ice—thus was done only at the end of the data collection process.

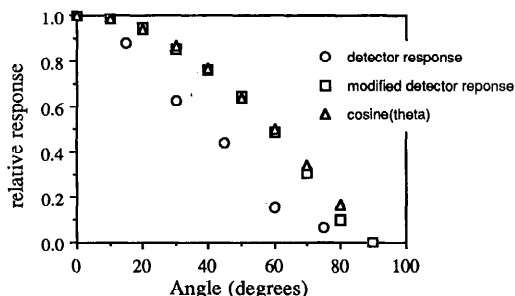


Fig. 3. Plot of cosine collector's response as a function of angle. Collector used in this experiment illustrated as the detector response. Collector has since been modified to obtain the response illustrated. Also shown is the ideal detector cosine response.

Ice crystal observation—Vertical and horizontal ice sections were taken to observe the ice crystal and brine cell structures. The ice consisted of vertical columns of crystals with horizontal diameters ranging from <1 mm to 0.5 cm. Column length ranged from 1 to 7 cm.

The beam spread function experiment

BSF definition—The beam spread function (BSF) is the optical analog of the electrical engineer's system impulse response or the physicist's Green's function. To define BSF consider an optical propagation path composed of scattering and/or absorbing media and/or optical elements such as lenses, etc. Illuminate the path with a perfectly collimated light beam of no angular divergence, i.e. the radiometric analog of a delta or impulse function. Energy is scattered as the beam propagates along the path. The irradiance distribution exiting the path represents path-introduced beam spreading. This distribution is defined as the path beam spread function, i.e. the path response to an impulse or pencil beam. Once the BSF is known, the path's response to any arbitrary distribution of input light, G , can be found by convolution of the BSF with G in real space.

The modulation transfer function (MTF) is the two-dimensional Fourier transform (the Hankel transform for systems with radial symmetry) of the BSF and provides a practical way of obtaining the BSF using a real Gaussian light beam rather than an ide-

Significant symbols

z	Ice thickness, cm
r	Radial distance from center of beam, cm
$E(r, z)$	Surface irradiance distribution, $\mu\text{W cm}^{-2} \text{nm}^{-1}$
$F(u, v)$	Two-dimensional Fourier transform of $E(z)$, dimensionless
u, v	Spatial frequencies in the x and y directions, cm^{-1}
w	Radial frequency, cm^{-1}
$H(w)$	Hankel transform, dimensionless
J_0	First-order Bessel function, dimensionless
k_M	Diffuse attenuation coefficient derived from MTF measurement, cm^{-1}
k_B	Peak attenuation coefficient of the BSF, cm^{-1}
σ	Beam spread coefficient, cm
θ	Zenith angle of radiance measurement, degrees
$L(\theta, z)$	Radiance distribution, $\mu\text{W cm}^{-2} \text{nm}^{-1} \text{sr}^{-1}$
k_L	Attenuation coefficient of peak radiance, cm^{-1}
$n(z)$	Exponential function for radiance distribution, dimensionless
$\langle r^2 \rangle^{1/2}$	Root-mean-square of the beam spread, cm

al light pencil. To use the MTF we measure the irradiance spread of the beam before it illuminates the path. The path is then illuminated and the exit irradiance measured. Both measured irradiances are transformed. The quotient of the exiting path irradiance transform divided by the beam transform is the MTF whose inverse transform is the path BSF.

BSF light collector apparatus—A motorized cart moved a small-aperture, downward-looking fiber-optics irradiance collector on a linear track slightly above and parallel to the ice surface (Fig. 1). Figure 3 illustrates the angular response of the cosine collector used. This device was similar to those used in underwater optics (Smith 1969). Since these measurements were made, the collector has been modified and tuned to obtain better cosine response as illustrated in the figure. Ice of thickness z (units given in list of symbols) was illuminated from below by the laser beam. The collector passed over the center of the exit beam and measured the irradiance along a radial line, r , of the circularly symmetric irradiance pattern, $E(r, z)$.

BSF measurement procedure—An observation sequence started with the measure-

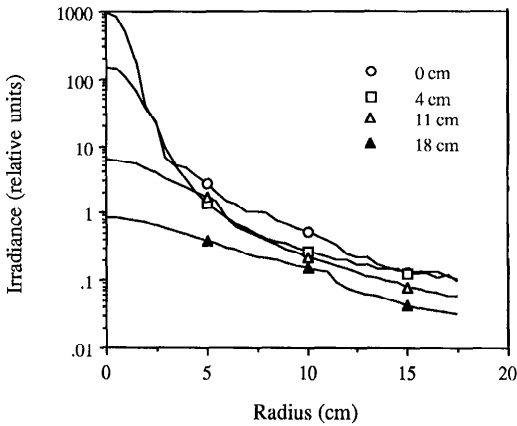


Fig. 4. Plot of the irradiances measured for various ice thicknesses in BSF experiment. General trend shows broadening of irradiance profile and decrease of peak value with increasing ice thickness.

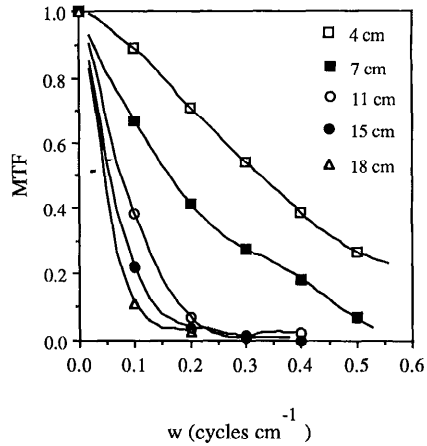


Fig. 5. MTF of the ice for different ice thicknesses, generated from the irradiance profiles in Fig. 4 as described in text. Figure shows decreasing value of MTF for higher spatial frequencies as ice thickness increases.

ment of the source pattern projected up through the water, $E(r, 0)$, in an ice-free tank. To do this, we cooled the room to -35°C and allowed a very thin layer of ice to form on the water surface. This first sheet was carefully and completely removed, guaranteeing a water surface free of debris, oil, and other contaminants. The source irradiance was then measured through this pristine water surface. Measurements were continued as the ice grew from 0 to 18 cm in thickness.

BSF data reduction—The inherent radial symmetry of the beam pattern simplified BSF data reduction. For a radially symmetric pattern, $E(r, z)$ [or in Cartesian coordinates, $E(x, y, z)$], the two-dimensional Fourier transform $F(u, v)$ of the pattern is related to the Hankel transform, $H(w)$, by the relationship $F(u, v) = 2\pi H(w)$ where $w = (u^2 + v^2)^{1/2}$ (Papoulis 1968). The source produced a radially symmetric irradiance, $E(r, z)$, for each ice thickness, z . Starting with the ice-free source irradiance scan, $E(r, 0)$, each $E(r, 0)$ was transformed with a finite Hankel transform, i.e.

$$H(w, z) = \int_0^{R_{\max}} rE(r, z)J_0(rw) dr$$

$$\approx \sum_0^{R_{\max}} rE(r, z)J_0(rw) \Delta r.$$

The relation $\text{MTF}(w, z) = H(w, z)/H(w,$

$0)$ then gave the MTF for each ice thickness, where $H(w, 0)$ was the ice-free source transform. Because real data mandates use of a finite Hankel transform, the MTF rang about the zero ordinate at higher frequencies. This was simply a Gibb's phenomenon artifact (Rabiner and Gold 1975) inherent in the truncation associated with the use of a finite transform on real data. To eliminate any potential singularities in the MTF and BSF that these oscillations about zero could cause, we used a high frequency cutoff of MTF corresponding to the first zero in the source Hankel transform, $H(w, 0)$. Additionally for the measured irradiance transforms, $H(w, z)$, amplitudes beyond the first-frequency zero crossing of each $H(w, z)$ were set equal to zero. These two editing changes reduced singularities introduced by artifacts of the computational method but reintroduced a slight Gibb's phenomenon in the BSF. The BSF(r, z) for each ice thickness z was then obtained by inverse transforming the computed $\text{MTF}(w, z)$.

Results and discussion—Measurements were made on ice as it grew over a 7-d period. Sampling was done at 0.25-cm separations (a Nyquist frequency of 2 cy cm^{-1}). Figure 4 shows the raw irradiance exiting the ice vs. radial distance as seen by the small Lambertian detector. The source irradiance through ice-free water is included. The ice MTF was the quotient of the Hankel

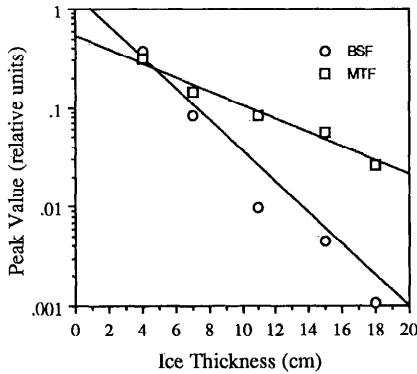


Fig. 6. Peak values of MTF and BSF vs. ice thickness. Lines are empirical fits to the data.

transforms of the measured irradiances through ice divided by the source Hankel transform. Figure 5 shows the ice MTF for thicknesses of 4, 7, 11, 15, and 18 cm. The thin-ice MTF had a wide bandwidth which allowed small details of the light field to be transmitted. As ice thickness increased so did multiple scattering, and the MTF changed in two significant ways. First, multiple scattering blurred spatial details of the beam. High spatial frequencies were attenuated and the ice MTF acted as a narrow low pass filter (Fig. 5) (i.e. MTF narrows with increased ice thickness). Second, photon pathlength was increased by multiple scattering, more light was absorbed, and the MTF magnitude at all frequencies was decreased. By definition the zero-frequency bin of the MTF measures the mean value of total energy at any ice thickness. The decrease of peak MTF magnitude with ice growth seen in Fig. 6 was treated as a diffuse attenuation coefficient, k_M , for the new ice. The diffuse attenuation coefficient k_M obtained from a regression fit (correlation coefficient = 0.97) of MTF peak over all ice thicknesses was 0.163 cm^{-1} . This coefficient was near the diffuse attenuation coefficient of 0.13 cm^{-1} measured by Perovich (1979) for light of 500-nm wavelength in a tank at -35°C .

The ice BSF was derived by inverse transforming the calculated ice MTF. Figure 7 shows the resulting ice BSF normalized to display shape. Figure 7 also shows Gibbs' phenomena oscillations due to the finite width of the calculated values of the MTF

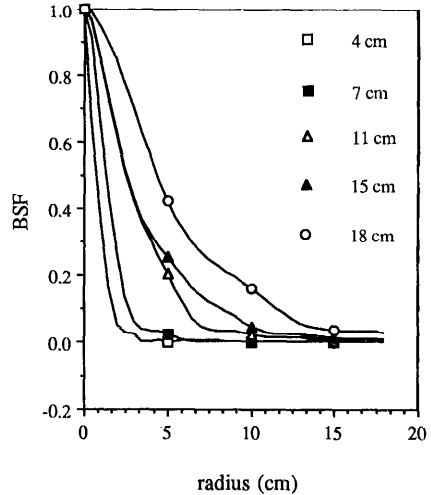


Fig. 7. BSF of the ice for different ice thicknesses normalized to the value on axis. These data are calculated from the Hankel transform of the MTF values illustrated in Fig. 5.

evident in the BSF wings. The central BSF peaks are attenuated with increasing ice growth. An average peak attenuation k_B was obtained by a regression fit of the central BSF peaks (correlation coefficient = 0.98). For our sample $k_B = 0.405 \text{ cm}^{-1}$. Figure 6 displays the regression fit to the measured peak BSF values for each ice thickness. The slope of the fit is k_B —the attenuation of the BSF peak value as the ice grows. As can be seen in Fig. 7 the BSF widened as the ice grew. The growth of beam spread with increasing ice thickness was studied by examining the root-mean-square spread at each ice thickness ($\langle r^2 \rangle^{1/2}$). This $\langle r^2 \rangle^{1/2}$ was calculated as the second moment of the beam spread function $\text{BSF}(r, z)$ at that thickness, i.e.

$$\langle r^2 \rangle^{1/2} = \left[\sum_n r_n^2 \text{BSF}(r_n, z) \right]^{1/2}.$$

Figure 8 displays $\langle r^2 \rangle^{1/2}$ in cm for each ice thickness. If the shape of the BSF is Gaussian then a plot of $\ln(\text{BSF})$ vs. r^2 should be linear with the slope proportional to σ^2 . These plots were made and indicated that the BSF should be expressed as the sum of two Gaussian distributions, one narrow of high amplitude and the second much wider with a low amplitude. Physically the narrow distribution was due to single and multiple

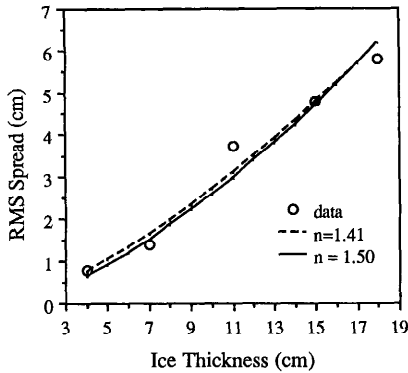


Fig. 8. $\langle r^2 \rangle^{1/2}$ spread vs. ice thickness (data points—O; the two experimental power law fits are illustrated as lines). The $n = 1.50$ fit is a single-parameter fit restricting the exponent to that theoretically predicted in the diffusion regime.

forward scattering of the direct beam in the ice. The second lower amplitude, wider field was attributed to the gradual increasing of multiply backscattered and forward scattered light producing a diffuse light field background in the ice. Within the first few scattering lengths the narrow field would be dominant, but as the ice thickens, more light from the narrow beam would be redistributed in the diffuse field until all light could be described solely by the wide distribution. As our measurements were of relatively thin, new ice this extreme diffuse condition was not observed and the narrow Gaussian spread of the main beam was not important. This narrow beam spread function was thus fit with a Gaussian curve of the form $BSF(r, z) = B \exp(-r^2/2\sigma^2)$ where B is a function

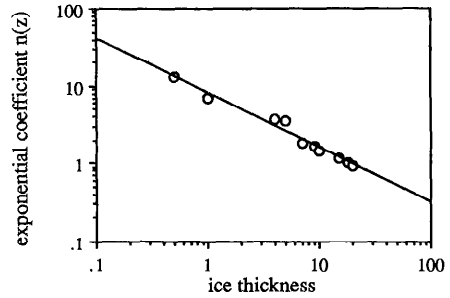


Fig. 10. Plot illustrating the variation of the exponential coefficient $[n(z)]$ with ice thickness, along with the empirical fit to this function. Exponential coefficients determined by fitting data shown in Fig. 9 to functions of the form $L(\theta) = \cos^{n(z)}(\theta)$.

of the irradiance level, and σ a function of thickness.

Arnush (1972) computed the spread of a Gaussian beam through a turbid media to vary as the $3/2$ power of the pathlength. We regressed $\langle r^2 \rangle^{1/2}$ in two ways to fit a power law of the form $A z^n$. The first regression solved for magnitude A and the exponent n . This regression gave an exponent $n = 1.41$ and an A of 0.105 (correlation coefficient of 0.98). The observed $n = 1.41$ differs from the 1.5 theoretically predicted by 6%. The second regression solved for the single parameter A , while setting $n = 1.5$ (correlation coefficient 0.96). The data and the two fits are shown in Fig. 8. Although the two-parameter fit ($n = 1.41$) gave a smaller mean-square residual error than the one-parameter fit ($n = 1.5$), it is obvious that the $n = 1.5$ fit is quite good. Further work

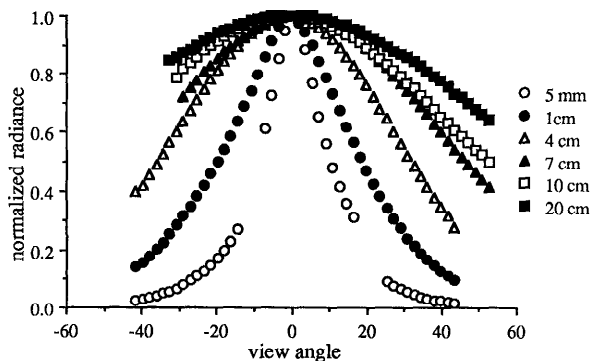


Fig. 9. Radiance distributions for the measured ice thicknesses, normalized to the value at 0° , and showing general trend toward flattening of the distribution with increasing ice thickness.

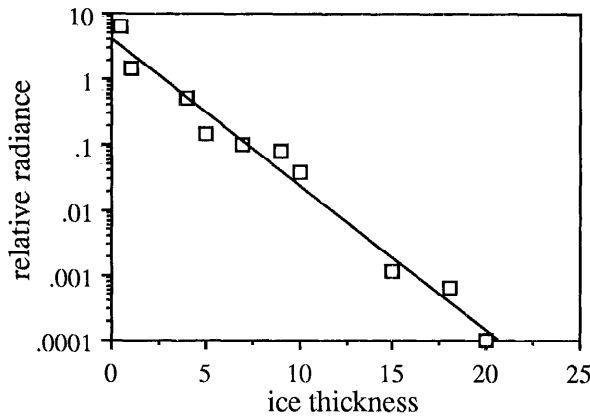


Fig. 11. Plot of peak value of radiance [$L(0)$] for different ice thicknesses; line is an empirical fit to the data. This plot was used to determine $k_t(z)$.

will examine whether ice grown at different air temperatures spreads light by the 1.5 exponential law. To summarize our BSF work, we have experimentally found a preliminary expression for $\langle r^2 \rangle^{1/2}$ of a beam passing upward through z cm of new ice grown at -35°C . This expression is

$$\langle r^2 \rangle^{1/2} = 0.105z^{1.41} \text{ cm.}$$

Thus for relatively thin, new ice the BSF is nearly Gaussian and can be approximated by

$$\text{BSF}(r, z) = \exp(-k_B z) \exp(-r^2/2\langle r^2 \rangle)$$

where $k_B = 0.404 \text{ cm}^{-1}$ is the measured BSF peak attenuation coefficient.

The beam scattering experiment

Definition of the forward scattered beam pattern—When a slab of ice is illuminated by a submerged light beam, the radiance exits the ice with some angular distribution dependent on the optical properties of the ice. This angular distribution is analogous to the angular beam pattern of a microwave radar. Knowledge of this scattered beam pattern is important in predicting the light received by an airborne radiance sensor some distance from the beam exit point on the ice surface. It can also provide information on the radiance distribution in the ice volume.

Apparatus—The forward scattering beam pattern was measured using a Gershun tube radiometer (full angle of 17°) mounted on a motorized cart traveling on a semicircular

gonio track above the cold room tank. The gonio track was mounted so that the radiometer was directed at the beam exit point on the ice below at all times. This instrument measured the angular distribution of radiance exiting the ice as the ice grew from 0 to 18 cm thick.

Results—The radiance distribution data for the angular range from zenith to 55° for the various ice thicknesses are shown in Fig. 9. In the figure the maximum value has been normalized to emphasize the change in shape of the scattered radiance with increasing thickness. As illustrated, increased ice thickness decreased variation in the radiance distribution. A candidate mathematical expression chosen to fit these data was

$$L(\theta, z) = L(0)\cos^{n(z)}(\theta)$$

where θ is the angle from zenith, z the ice thickness, and $n(z)$ a function of ice thickness. The $L(\theta, z)$ data for each z was regressed against θ to determine the $n(z)$ for that z . For the entire set of ice thicknesses, no correlation coefficient was < 0.92 . The resulting cosine exponent function $n(z)$ was regressed against ice thickness z (correlation coefficient = 0.98, Fig. 10). This exponent function is given by

$$n(z) = 8.022z^{-0.705}. \quad (1)$$

Thus, the angular distribution of scattered light can be predicted given ice thickness.

The peak value of scattered radiance with ice thickness was described by a regular attenuation function of the form

$$L(0, z) = L(0, 0)\exp(-k_L z).$$

A plot of the peak value of the radiance, $L(0, z)$, against ice thickness (Fig. 11) was fit by the above equation with a value of $k_L = 0.2229$ (correlation coefficient of 0.98).

These two empirical expressions allow the radiance field of light emitted from the ice surface when illuminated by an upward projected light beam to be completely described. In summary, the angular distribution of radiance L with angle θ and ice thickness z is

$$L(\theta, z) = L(0, 0)\exp(-k_L z)\cos^{n(z)}\theta$$

with $n(z)$ given by Eq. 1 and k_L given above.

Conclusions and future work

These results demonstrate that salt ice resembling new sea ice observed in Arctic regions can be grown and measured in a laboratory environment. Measurements of underwater, through-ice laser beam spreading and beam pattern have been made for a single sequence of ice grown from 0 to 18 cm thick. For this single growth sequence

we have described our results in terms of simple functions that can be used for estimating beam transmission and spreading. Further measurements are needed and will be performed to determine the sensitivity of these functions to growth conditions, ice morphology, and other physical parameters.

References

- ARNUSH, D. 1972. Underwater light-beam propagation in the small-angle scattering approximation. *J. Opt. Soc. Am.* **6**: 1109-1111.
- PAPOULIS, A. 1968. *Systems and transforms with applications in optics*. McGraw-Hill.
- PEROVICH, D. K. 1979. Optical properties of young sea ice. M.S. thesis, Univ. Washington. 151 p.
- , G. A. MAYKUT, AND T. C. GRENFELL. 1986. Optical properties of ice and snow in the polar ocean. 1: Observations, p. 232-241. *In Ocean Optics 8, Proc. SPIE 637*.
- RABINER, L. R., AND B. GOLD. 1975. *Theory and application of digital signal processing*. Prentice-Hall.
- SMITH, R. C. 1969. An underwater spectral irradiance collector. *J. Mar. Res.* **27**: 341-351.
- WEEKS, W. F., AND S. F. ACKLEY. 1986. Growth structure and properties of sea ice, p. 9-164. *In N. Untersteiner [ed.], Geophysics of sea ice*. Plenum.